From atomic-scale understanding to wafer-scale growth: Delta-doped AlN/GaN/AlN XHEMTs on single-crystal AlN by molecular beam epitaxy

Cite as: APL Mater. 13, 121103 (2025); doi: 10.1063/5.0300068
Submitted: 30 August 2025 • Accepted: 12 November 2025 •
Published Online: 1 December 2025

Yu-Hsin Chen,[1,a] Keisuke Shinohara,[2] Jimy Encomendero,[3] Naomi Pieczulewski,[1] Kasey Hogan,[4] James Grandusky,[4] David A. Muller,[5,6] Huili Grace Xing,[1,3,6] and Debdeep Jena[1,3,6,b]

AFFILIATIONS

[1] Department of Materials Science and Engineering, Cornell University, Ithaca, New York 14853, USA
[2] Teledyne Scientific Company, LLC, Thousand Oaks, California 91360, USA
[3] School of Electrical and Computer Engineering, Cornell University, Ithaca, New York 14853, USA
[4] Crystal IS, Inc., Green Island, New York 12183, USA
[5] School of Applied and Engineering Physics, Cornell University, Ithaca, New York 14853, USA
[6] Kavli Institute at Cornell for Nanoscale Science, Cornell University, Ithaca, New York 14853, USA

[a] **Author to whom correspondence should be addressed:** yc794@cornell.edu
[b] **Electronic mail:** djena@cornell.edu

ABSTRACT

The development of large-wafer single-crystal AlN substrates has expanded their role beyond UV photonics to enable next-generation integrated electronics. In this study, we investigated δ-doped AlN/GaN/AlN heterostructures, where an n-type δ-doping layer is introduced to suppress the undesired two-dimensional hole gas at the bottom GaN/AlN interface, thereby enhancing the conductivity of the two-dimensional electron gas at the top AlN/GaN interface. We began by systematically identifying epitaxial growth conditions to achieve high crystalline quality, as confirmed by cross-sectional transmission electron microscopy images. To understand the impact of δ-doping density on transport properties, we combined theoretical modeling with experimental measurements, revealing that an optimal δ-doping density of $\sim 5 \times 10^{13}$ cm^{-2} minimizes interface roughness scattering and enhances mobility. Finally, we demonstrated scalability by extending the growth to large-area wafers, supported by structural and transport characterization. A sheet resistance of 246.8 ± 38.1 Ω/□ measured across a 3-in. (75 mm) wafer highlights the uniformity and performance potential of δ-doped AlN/GaN/AlN heterostructures for high-power, high-frequency electronic applications.

I. INTRODUCTION

Aluminum nitride (AlN) has an ultrawide bandgap of 6 eV, high thermal conductivity of ~ 340 W/m K,[1] and high electrical insulation, which are the desired material properties for ultra-wide bandgap photonics and electronics applications. Driven by this potential, the development of single-crystal AlN substrates has rapidly progressed. Since 2021, high-quality 2-in. AlN substrates have entered robust mass production.[2,3] This was soon followed by the introduction of 3-in. AlN substrates.[4] More recently, advances in physical vapor transport growth techniques have enabled the development of 4-in. (100 mm) AlN substrates with a useable area exceeding 99%.[5] Initially, bulk AlN substrates were primarily used in ultraviolet (UV) photonics, particularly in the UVC region

(wavelength below 280 nm) for devices such as light emitting diodes and laser diodes.[6] At present, bulk AlN substrates have expanded their application into transistors and integrated electronics.[7–13]

AlN and GaN, both belonging to the wurtzite crystal family, can form AlN/pseudomorphically strained GaN/AlN heterostructures that support a high-density polarization-induced two-dimensional electron gas (2DEG). The large conduction band offset between AlN and GaN acts as an effective barrier to confine electrons. In addition, the AlN buffer layer removes the need for compensation doping to prevent buffer leakage and acts as a heat sink during device operation. For example, the AlN/GaN/AlN heterostructure can consist of a 5–20 nm pseudomorphically strained GaN channel under −2.4% compressive strain, and a ∼5 nm AlN barrier remains strain-free due to lattice matching with the AlN substrate. When epitaxially grown on single-crystal AlN substrates, these structures exhibit a million-fold reduction in dislocation density, down to $\approx 10^4$ cm^{-2}, along with the elimination of thermal boundary resistance between the buffer and substrate.[14] Recently, such AlN double heterostructures have also been achieved on various platforms such as SiC, sapphire, or Si substrates, using different epitaxial growth techniques.[11,13,15–17] The combined advantages make AlN-based HEMTs highly promising for high-power and high-frequency microwave electronics.

Unlike conventional AlGaN/GaN heterostructures on GaN, AlN/GaN/AlN double structures on AlN host immobile negative polarization sheet charges at the bottom GaN/AlN interface, which induce a two-dimensional hole gas (2DHG) confined by the valence band offset between AlN and GaN.[18] This leads to several drawbacks: (1) The presence of an additional polarization effect increases the internal electric field in the GaN channel, pushing the 2DEG closer to the interface and enhancing electron scattering.[19,20] (2) The empty electron states (holes in 2DHG) in the valence band can trap electrons from the channel, degrading current and limiting the transistor's output power.[21–24] In Ref. 25, we confirmed the existence of a 2DHG in the undoped AlN/GaN/AlN through capacitance–voltage (C–V) measurements on an on-wafer diode. The C–V profile of the undoped sample shows a two-step behavior, with an additional capacitance plateau at a depth corresponding to the centroid of the 2DHG following the initial depletion.

In our earlier study, we demonstrated that inserting a sheet of silicon donors at the bottom GaN/AlN interface eliminates the 2DHG and, therefore, reduces the internal electric field in the well.[26] This new device structure—δ-doped AlN/GaN/AlN on bulk AlN substrates, hereafter called the XHEMT [single-crystal (Xtal) high electron mobility transistor]—achieves a 2X higher 2DEG conductivity than its undoped counterpart. The C–V measurement of δ-doped XHEMT confirms the charge compensation. With a single electron channel and no 2DHG, the capacitance sharply decreases at the threshold voltage as the 2DEG is depleted.[25] The high-quality 2DEGs in the XHEMT heterostructure were confirmed by the observation of Shubnikov–de Haas oscillations.[27] Furthermore, we presented the DC and RF characteristics of the XHEMT, achieving an output power density of 5.92 W/mm in continuous wave operation with an associated power-added efficiency of 65% at 10 GHz.[25,28] The initial demonstrations were restricted to small-area samples of 1 cm^2. To further advance AlN-based XHEMT technology, finding the heterostructure design space and scaling epitaxial growth to large-area wafers are critical for accelerating research and enabling a production-compatible fabrication flow. In this study, we (1) develop and demonstrate optimized epitaxial growth conditions and microscopic analysis of the XHEMT structure, (2) identify the optimal δ-doping density for transport properties, and (3) scale the XHEMT growth to large-area bulk AlN wafers and report the resulting structural and transport properties.

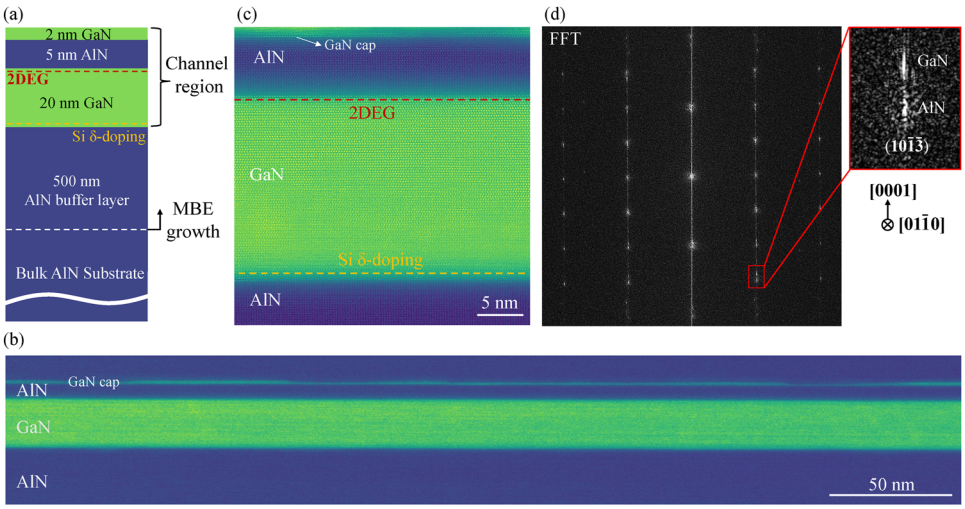

FIG. 1. (a) Schematic of the δ-doped AlN/GaN/AlN heterostructure on a bulk AlN substrate. A sheet of silicon donors with a nominal doping density of $\sigma_\delta = 4 \times 10^{13}$ cm^{-2} is incorporated at the bottom GaN/AlN interface, ∼26 nm below the surface. (b) A wide-view STEM image showing a thin 20 nm GaN channel sandwiched between an AlN buffer and an AlN barrier. (c) Atomic resolution ADF-STEM image shows an atomically sharp top interface between AlN/GaN and a ∼1 nm diffuse transition at the bottom GaN/AlN interface. This unintentionally graded interface was also observed in the STEM images of the undoped sample, indicating that it is not caused by δ-doping. (d) Fast Fourier transform (FFT) analysis of (b) shows that the diffraction peaks of GaN are coherently strained to AlN in the in-plane direction.

II. EPITAXIAL GROWTH

Figure 1(a) presents a schematic cross section of the XHEMT heterostructures of this study. They were grown using a Veeco GEN10 molecular beam epitaxy (MBE) system, equipped with a nitrogen RF plasma source and standard effusion cells for Al, Ga, and Si. In situ monitoring of film growth was conducted using a KSA Instruments reflection high-energy electron diffraction (RHEED) system with a Staib electron gun operating at 14.5 kV and 1.45 A. Growth temperatures were measured with a thermocouple positioned on the backside of the substrate. The XHEMT structures were grown on single-crystal AlN substrates from Crystal IS with a dislocation density of less than 10^4 cm^{-2}. The substrates were initially cleaned ex situ using solvents and acids, followed by overnight outgassing at 200 °C in the MBE load-lock chamber. Before epitaxial growth, *in situ* Al-assisted cleaning was performed to remove native surface oxides and ensure a clean, epi-ready starting surface.[29,30] A 500 nm AlN buffer layer was grown under metal-rich conditions at a constant thermocouple temperature of T_c = 1060 °C to ensure high crystallinity. After growth, excess Al droplets were thermally desorbed *in situ* by raising the thermocouple temperature by 50 °C. Subsequently, the substrates were cooled down to 850 °C to prepare for the growth of the channel region.

The channel region, consisting of a 20 nm GaN layer with silicon δ-doping, a 5 nm AlN barrier, and a GaN capping layer, was grown continuously without any growth interruptions. Metal-rich growth conditions to maintain step-flow growth mode were used throughout the entire epitaxial process to achieve atomically smooth interfaces and surfaces. Beam equivalent pressures (BEPs) were set at 1.5×10^{-6} Torr for Ga during the growth of the GaN channel and cap layers and 2.5×10^{-7} Torr for Al during the growth of the AlN barrier layer. The RF power of 200 W and nitrogen flow rate of 0.35 sccm were used, corresponding to an N flux of 1.8×10^{-7} Torr and a growth rate of 3.1 nm/min. During growth, the substrate was rotated at 20 rpm, yielding an effective growth rate of 0.6 monolayers per rotation. The δ-doping condition was calibrated using a separate MBE-grown silicon-doped GaN sample with a silicon cell temperature of T_{Si} = 1300 °C, yielding a 3D doping density of 4.86×10^{19} cm^{-3}.

In this study, a 20 nm GaN channel was chosen to maintain coherent strain with the AlN substrate. The 5 nm AlN barrier remains strain-free and, due to the large polarization discontinuity between GaN and AlN, induces a high 2DEG density. Our previous study demonstrated that the combination of a 20 nm GaN channel and a 5–6 nm AlN barrier yields a low sheet resistance.[20,26] A 2 nm GaN cap layer was subsequently grown to prevent oxidation of the underlying AlN barrier. In addition, the GaN cap thickness plays a role in modulating the 2DEG density in the AlN/GaN/AlN heterostructure due to polarization and band discontinuity. Increasing the thickness of the GaN cap results in a reduction in 2DEG density, highlighting its influence on the electrostatics of the heterostructure.

Figure 2 shows the shutter on/off timing sequence and substrate temperature during the growth of the XHEMT channel region. This process began by opening the Ga shutter for 30 s to form Ga adlayers, enhancing adatom diffusivity. Both Ga and N shutters were then opened to deposit a 1 nm thick GaN spacer layer, followed by silicon δ-doping at T_{Si} = 1300 °C for the time needed to incorporate a sheet of silicon donors with δ-doping density of $\sigma_\delta = 4 \times 10^{13}$ cm^{-2}.

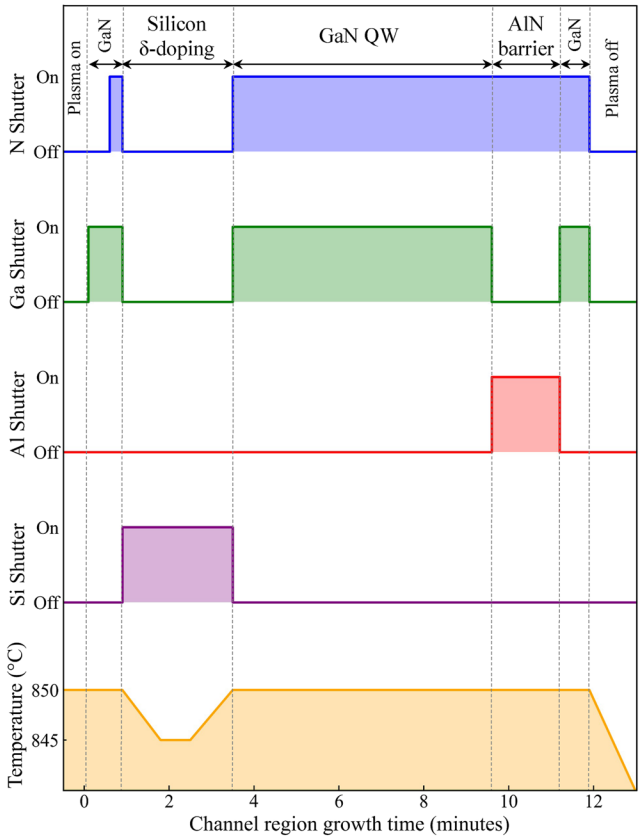

FIG. 2. Shutter on/off status for N, Ga, Al, and Si sources, together with substrate temperature, plotted as a function of time during the uninterrupted growth of the channel region, which consists of a silicon δ-doped GaN channel, an AlN barrier, and a GaN capping layer. The growth began with a 1 nm GaN layer, followed by δ-doping, during which only the Si shutter was opened while the N plasma remained on and all other shutters were closed. During this step, the thermocouple temperature was reduced by 5 °C to prevent surface drying. Immediately after δ-doping, growth resumed continuously with the remaining GaN channel, the AlN barrier, and the GaN cap at 850 °C.

During δ-doping (see on/off plot in Fig. 2), the nitrogen plasma remained on, with only the silicon shutter open and others closed, while the thermocouple temperature was lowered by 5 °C to prevent the surface from drying. After δ-doping, the Si shutter was closed, and the Ga and N shutters were reopened promptly to resume the growth of the remaining GaN channel, followed by the AlN barrier and GaN cap. After epitaxial growth, the nitrogen plasma was turned off, and the samples were cooled down to room temperature (RT) immediately. The excess Ga droplets were then removed ex situ using HCl.

III. RESULTS AND DISCUSSIONS

A. TEM analysis

To investigate the coherence and interface quality of the XHEMT structure, a cross-sectional TEM specimen was prepared using a Thermo Fisher Helios G4 UX focused ion beam with a

final milling step of 5 keV to reduce damage. The sample was then examined with an aberration-corrected Thermo Fisher Spectra 300 CFEG operated at 300 keV. Figure 1(b) presents a wide-view STEM image of a thin 20 nm GaN channel sandwiched between an AlN buffer and an AlN barrier. Figure 1(c) shows the image of the lattice-matched XHEMT heterostructure at atomic resolution obtained by annular dark-field scanning transmission electron microscopy (ADF-STEM). The top AlN/GaN interface, where the 2DEG resides, shows an abrupt and smooth interface, in contrast to the ~1 nm gradient interface observed at the bottom GaN/AlN interface. While the origin of this unintentionally graded interface is still under investigation, it may result from group III vacancies generated during high-temperature AlN buffer growth, which facilitate interatomic diffusion during the subsequent low-temperature GaN channel growth, as previously reported.[13,31] This unintentionally graded interface was also observed in the STEM images of the undoped sample, indicating that it is not caused by δ-doping. A fast Fourier transform (FFT) analysis of Fig. 1(b) reveals the distinct high-order diffraction peaks from both AlN and GaN, as shown in Fig. 1(c). The vertical alignment of the diffraction peaks indicates that the 20 nm GaN channel remains coherently strained to the AlN substrate.

B. Investigate δ-doping density

Figure 3 shows the energy band diagrams and carrier density profiles of XHEMTs at increasing δ-doping densities, calculated by a self-consistent 1D Schrödinger–Poisson solver, assuming full ionization. The δ-doping was introduced after 1 nm of GaN, ~26 nm below the surface. As shown in Fig. 3(a), the undoped AlN/GaN/AlN heterostructure forms a 2DEG at the top AlN/GaN interface, while a 2DHG with a density of $p_s = 3.86 \times 10^{13}$ cm^{-2} coexists in the GaN channel at the bottom GaN/AlN interface. In Fig. 3(b), introducing a δ-doping density of $\sigma_\delta = 4 \times 10^{13}$ cm^{-2} reduces the 2DHG density by two orders of magnitude but does not entirely eliminate it. In Fig. 3(c), increasing the doping density to $\sigma_\delta = 5 \times 10^{13}$ cm^{-2} shifts the valence band edge E_V completely below the Fermi level E_F, ensuring that E_F remains within the energy gap and thereby suppressing 2DHG formation. Further increasing the doping density to $\sigma_\delta = 6 \times 10^{13}$ cm^{-2} is counterproductive: it causes E_C to cross below E_F ($E_C < E_F$) at the δ-doping plane, leading to a second electron channel formation, as shown in Fig. 3(d).

The average electric field F_{avg}, weighted by the electron density distribution in the triangular quantum well, is given by $F_{avg} = \frac{\int n(z) \times F(z)\, dz}{\int n(z)\, dz}$, where $n(z)$ and $F(z)$ are the position-dependent electron density and electric field, respectively, and are obtained from the self-consistent Schrödinger–Poisson solver. As the δ-doping density increases, F_{avg} decreases from 3.5 MV/cm in the undoped structure to 2.47 MV/cm at a δ-doping density of $\sigma_\delta = 5 \times 10^{13}$ cm^{-2}, where the 2DHG is fully removed. Beyond this doping density, F_{avg} saturates at 2.39 MV/cm, as both the local electric field and 2DEG density in the triangular quantum well reach their respective saturation limits. The reduction in electric field is evident in the energy band diagram of Fig. 3, where the conduction band exhibits a decreasing slope with increasing δ-doping density.

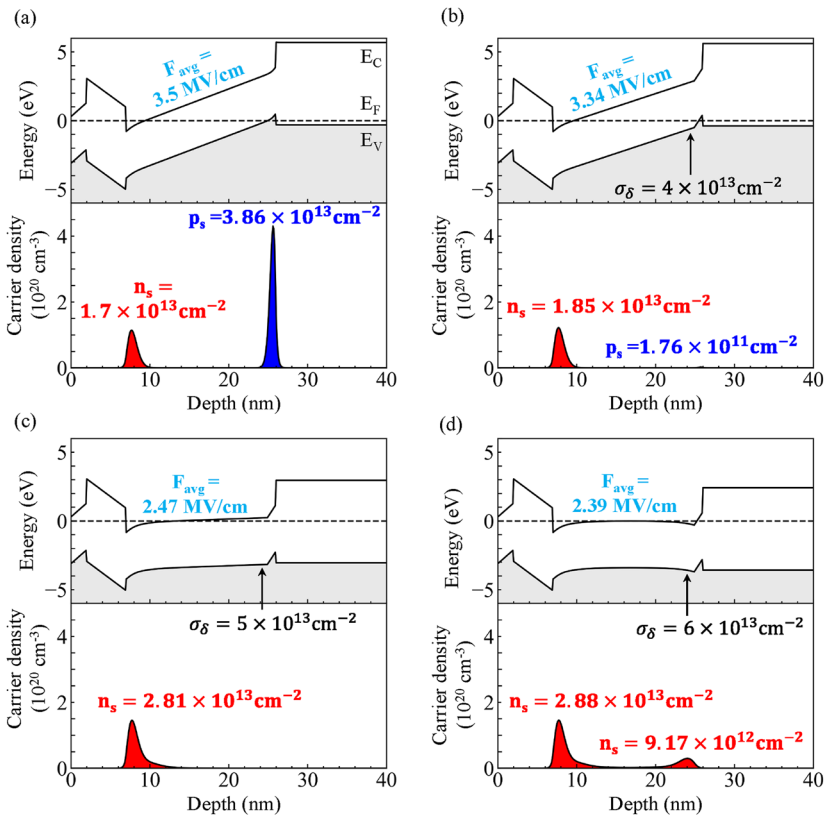

FIG. 3. Calculated energy band diagrams and carrier density profiles of δ-doped AlN/GaN/AlN heterostructures at different δ-doping densities. The average electric field F_{avg} is weighted by the electron density distribution in the triangular quantum well. (a) In the undoped AlN/GaN/AlN heterostructure, 2DEG and 2DHG coexist in the GaN channel. (b) Introducing a δ-doping density of $\sigma_\delta = 4 \times 10^{13}$ cm^{-2} reduces the 2DHG density by two orders of magnitude. (c) Increasing to $\sigma_\delta = 5 \times 10^{13}$ cm^{-2} completely eliminates the 2DHG by pushing E_V farther below E_F. (d) At $\sigma_\delta = 6 \times 10^{13}$ cm^{-2}, E_C falls below E_F at the δ-doping plane, resulting in the formation of a second electron channel.

Guided by these calculations, a series of samples with varying nominal δ-doping density σ_δ were grown. Figures 4(a) and 4(b) and Table I show the transport properties of these samples. By the nominal δ-doping density, we refer to the targeted δ-doping density during epitaxial growth. The precise silicon concentration at the bottom GaN/AlN interface was determined by secondary ion mass spectrometry (SIMS) measurements, which will be discussed in Sec. III C.

Figure 4(a) presents the experimentally measured 2DEG density of these samples alongside calculated values as a function of δ-doping density σ_δ. The experimental data exhibit a similar trend to the calculated values. Low δ-doping densities initially fall within the compensation region, where electrons from silicon compensate 2DHG, resulting in only a slight increase in 2DEG density. Once the δ-doping density exceeds $\sigma_\delta = 4 \times 10^{13}$ cm^{-2}, the calculated 2DEG density increases linearly with nominal doping density, with a slope of ~1. In this regime, excess electrons migrate to the triangular quantum well and the surface. Those in the well become confined and contribute to conduction, marking the transition to the modulation doping regime. When the δ-doping density $\sigma_\delta \geq 5.5 \times 10^{13}$ cm^{-2}, causing E_C to fall below E_F at the δ-doping plane [see Fig. 3(d)], the 2DEG density in the triangular well saturates, while the integrated sheet carrier density continues to increase due to the formation of a second electron channel.

Figure 4(b) shows the measured mobility vs 2DEG density at both 300 and 77 K. As the δ-doping density increases, the mobility at 300 K increases from 688 cm^2/Vs in the undoped structure to a peak of 802 cm^2/Vs at a doping density of $\sigma_\delta = 5 \times 10^{13}$ cm^{-2}. Further increasing the δ-doping density to $\sigma_\delta = 6 \times 10^{13}$ cm^{-2} leads to a decline in mobility to 699 cm^2/Vs. A similar trend is observed at 77 K. As the 2DEG density increases, the sheet resistance at 300 K decreases from 535 Ω/□ in the undoped sample to 299 Ω/□ in the most heavily doped sample. The low sheet resistance at high doping levels is attributed to the high 2DEG density, resulting from the formation of a second electron channel.

The non-monotonic trend in mobility with increasing 2DEG density (or δ-doping density) can be explained by analyzing the mobility-limiting scattering mechanisms, as shown in Fig. 4(c). The analysis considers acoustic phonon (AP),[32] polar optical phonon (POP),[33] interface roughness (IR),[34,35] remote ionized impurity scattering (Imp),[36] and parallel conduction when a second channel is present at the bottom GaN/AlN interface. Among these, the calculated mobility limited by Imp scattering is on the order of 10^6, which is far outside the range shown in Fig. 4(c). At 300 K, mobility is

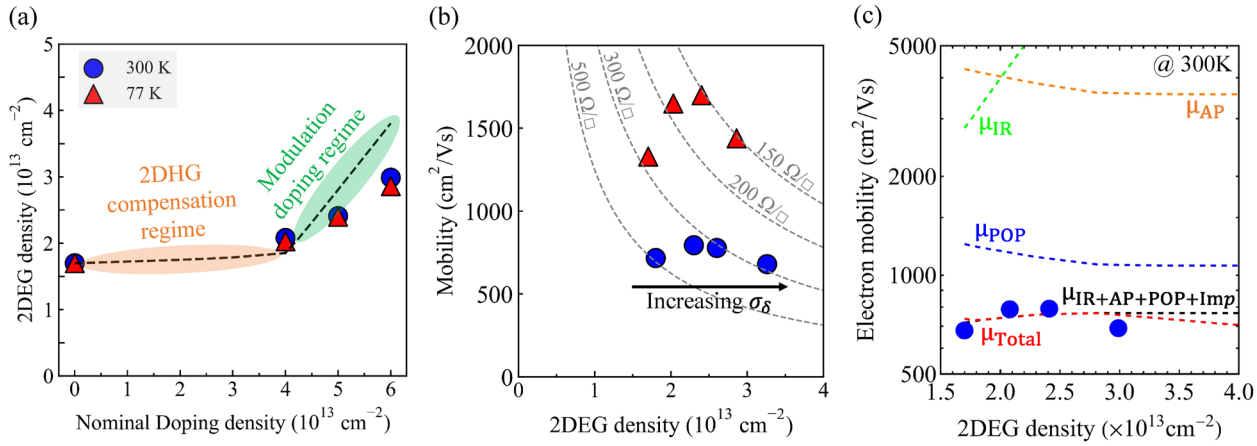

FIG. 4. Transport properties at both 300 and 77 K for a series of samples with different nominal δ-doping densities σ_δ. (a) Measured 2DEG density (solid symbols) and the corresponding calculated values (dashed line) as a function of σ_δ. (b) Mobility vs 2DEG density for samples with different σ_δ. (c) Theoretical modeling of mobility vs 2DEG density. The black line is the total scattering-limited mobility calculated using Matthiessen's rule, combining contributions from acoustic phonon scattering (μ_{AP}, orange dashed line), polar optical phonon scattering (μ_{POP}, blue dashed line), interface roughness scattering (μ_{IR}, green dashed line), and remote ionized impurity scattering (not shown because $\mu_{Imp} \sim 10^6$ is out of the range). The red dashed line μ_{Total} includes the combined effects of $\mu_{IP+AP+POP+Imp}$ (black dashed line) with the impact from parallel conduction (as a fitting parameter) when a second channel is present at the bottom GaN/AlN interface.

TABLE I. Measured 2DEG densities (n_s), mobilities (μ), and sheet resistances (R_s) for samples with varying nominal δ-doping densities (σ_δ) at 300 and 77 K.

Sample	σ_δ (10^{13} cm^{-2})	$n_s^{300\ K}$ (10^{13} cm^{-2})	$\mu^{300\ K}$ (cm^2/Vs)	$R_s^{300\ K}$ (Ω/□)	$n_s^{77\ K}$ (10^{13} cm^{-2})	$\mu^{77\ K}$ (cm^2/Vs)	$R_s^{77\ K}$ (Ω/□)
A	0	1.70	688	535	1.70	1330	277
B	4	2.08	798	376	2.03	1650	186
C	5	2.41	802	323	2.40	1700	143
D	6	2.99	699	299	2.86	1440	151

predominantly limited by POP scattering, with its strength rising as 2DEG density increases.

IR scattering, on the other hand, strongly depends on both the internal electric field ($\mu_{IR} \propto 1/F_{avg}^2$) and the screening factor. The statistical properties of IR are characterized by the correlation length (Λ) and the roughness amplitude (δ). In this calculation, Λ is set to 1.25 nm, which is close to the lateral interface roughness reported for AlGaN/GaN.[37] The value of δ is fixed at 0.17 nm for all samples, which is of the same order of magnitude as the experimentally measured RMS roughness. As shown in Fig. 4(c), the influence of IR scattering decreases with increasing δ-doping density due to the reduction in internal electric field and improved screening from the higher 2DEG density.

In Fig. 4(c), the black dashed line represents the combined mobility limited by IR, AP, POP, and Imp scattering, showing that the initial increase in mobility is driven by reduced IR scattering. However, the final mobility should account for parallel conduction arising from the presence of a 2DHG in the undoped structure or from an additional electron channel in the over-doped structure. The red dashed line represents the total mobility considering both scattering-limited mobilities and parallel conduction, which is given by $\mu_{parallel} = \frac{\sigma_1\mu_1+\sigma_2\mu_2}{\sigma_1+\sigma_2}$, where σ_i and μ_i are the conductivity and mobility of each channel, respectively.[38] When modeling parallel conduction, carrier densities for both channels were determined using a self-consistent Schrödinger–Poisson solver. The 2DHG mobility (μ_{2DHG} = 8.9 cm^2/Vs) was experimentally measured from a GaN/AlN sample grown by MBE under the same conditions as the undoped sample but without the top barrier, whereas the mobility of the second electron channel ($\mu_{parallel\ electron}$ = 350 cm^2/Vs) was treated as a fitting parameter. As shown by the red line, the total mobility falls below the black dashed line at high 2DEG densities due to parallel conduction from the undesired second electron channel. This theoretical model was also applied at 77 K, where mobility is primarily limited by IR and AP scattering. As shown in Fig. S1 of the supplementary material, the initial increase in mobility as 2DEG density (or δ-doping density) increases is due to the reduction in IR scattering. Overall, the model captures the measured mobility trend across samples with varying δ-doping densities.

Fully understanding the impact of different δ-doping densities on device performance remains an important area for future study. By combining experimental results with simulations, an optimal δ-doping density range of σ_δ = 4.5–5 × 10^{13} cm^{-2} is identified

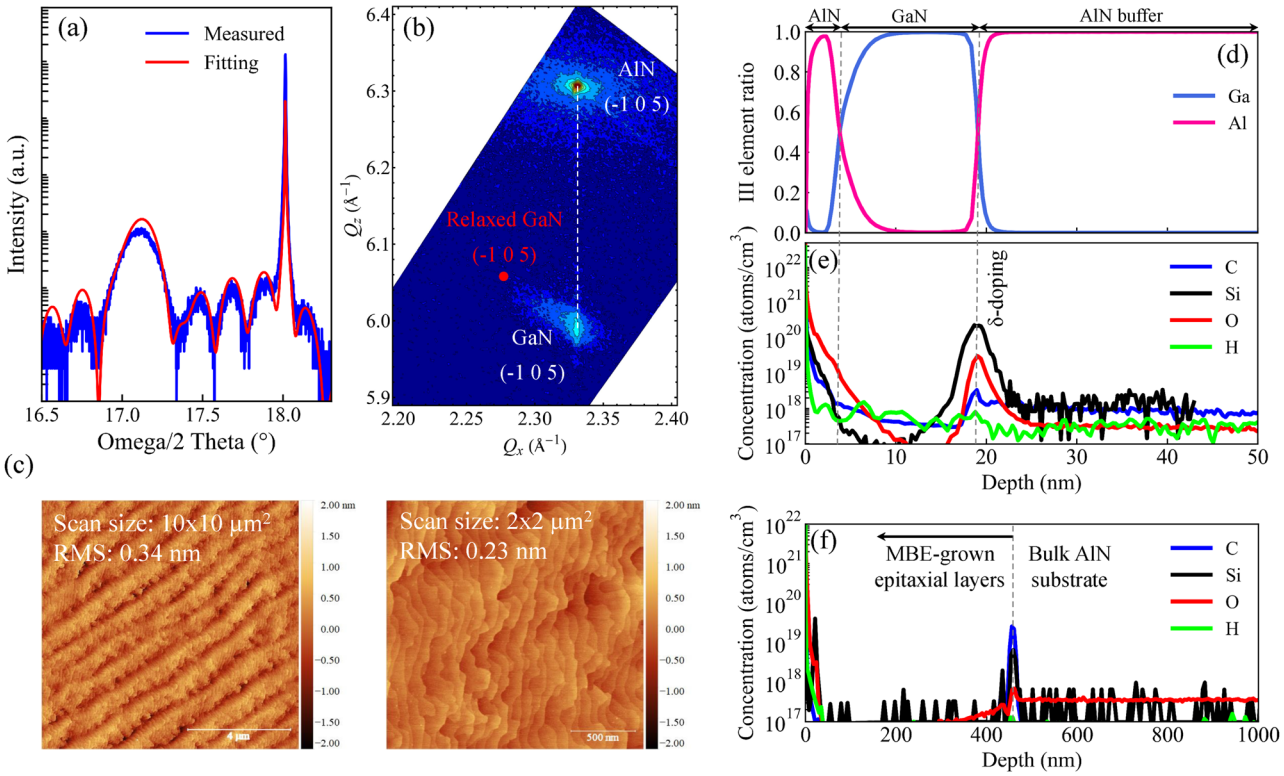

FIG. 5. Structural characterization of a 2-in. δ-doped AlN/GaN/AlN on a bulk AlN substrate. (a) Measured (blue) and simulated (red) omega/2theta x-ray diffraction scans across the symmetric (002) reflection confirm the target thickness and sharp interfaces. (b) X-ray reciprocal space mapping (RSM) around the asymmetric (−105) reflection confirms that the GaN layer is coherently strained to the AlN substrate. (c) AFM scans over 10 × 10 and 2 × 2 μm^2 areas reveal smooth surface morphologies with atomic steps. Secondary ion mass spectrometry (SIMS) analysis shows (d) the group III element ratio; (e) impurity concentrations in the channel region (shallow profile down to 50 nm), where the integrated sheet silicon concentration is σ_δ = 5 × 10^{13} cm^{-2}; and (f) impurity concentrations in the deep profile extending into the bulk AlN substrate, with the peak concentrations of carbon, silicon, and oxygen ~2.3 × 10^{19}, 5.2 × 10^{18}, and 5.5 × 10^{17} atoms/cm^3, respectively, and all decay to background levels within 50 nm of the epitaxial layers.

to compensate the 2DHG without creating parallel conduction in the XHEMT structure.

C. Large-area wafer growth

XHEMT heterostructures were grown on 2-in. and 3-in. bulk AlN substrates using the optimized growth conditions and a targeted δ-doping density of $\sigma_\delta = 4 \times 10^{13}$ cm^{-2}. The heterostructure details of the wafer are shown in Fig. 1(a). The structural quality of the 2-in. XHEMT wafer was assessed using high-resolution x-ray diffraction with a Panalytical Empyrean® diffractometer emitting Cu Kα_1 radiation. Figure 5(a) shows the measured diffraction pattern at the wafer center around the (002) symmetric reflection, along with theoretical diffraction patterns calculated using a dynamical diffraction model. The well-resolved interference fringes indicate sharp heterointerfaces, and the good agreement between measured and calculated patterns allows for precise thickness extraction. Reciprocal space mapping around the asymmetric (−105) diffraction in Fig. 5(b) confirms a coherently strained GaN on AlN. Surface morphology at the wafer center was characterized using atomic force microscopy (AFM) with an Asylum Research Cypher ES setup. Figure 5(c) reveals smooth surface morphology with atomic steps and sub-nanometer root mean square (rms) roughness.

SIMS analysis on a 1 × 1 cm^2 piece of the 2-in. XHEMT wafer was performed by the Evans Analytical Group to investigate the silicon δ-doping level and impurity incorporation. Figure 5(d) presents the group III element ratio in the XHEMT heterostructure, confirming the presence of a binary GaN channel and AlN barrier. Figure 5(e) shows a shallow SIMS profile down to 50 nm, capturing impurity concentrations in the channel region. From SIMS analysis of the XHEMT sample, the integrated sheet silicon concentration at the GaN/AlN interface is $\sigma_\delta = 5 \times 10^{13}$ cm^{-2}. This value is 1×10^{13} cm^{-2} higher than the nominal target due to unintentional silicon incorporation at the growth interface, as confirmed by SIMS analysis of the undoped structure. Nevertheless, the measured silicon concentration remains within the optimal δ-doping range. The observed broadening of the silicon profile into the AlN buffer may be a SIMS measurement artifact, where the primary ion beam pushes atoms into the AlN layer. For unintentional impurities at the GaN/AlN interface, the integrated sheet concentrations for oxygen and carbon are ~6.9×10^{12} and 3.8×10^{11} atoms/cm^2, respectively. The oxygen concentration peak of density ~10^{19} cm^{-3} observed near the δ-doping region is possibly due to the growth interruption following the AlN buffer layer. This interruption is necessary to desorb excess Al. During this interruption, oxygen-containing species likely adsorb onto the surface and are incorporated once growth resumes, resulting in the observed concentration peak. Figure 5(f) provides a deeper SIMS profile into the bulk AlN substrate, showing that the impurity concentrations remain close to or below detection limits throughout the 500 nm epitaxial AlN buffer layer. At the growth interface between the epitaxial layers and the substrate, the peak concentrations of carbon, silicon, and oxygen are ~2.3×10^{19}, 5.2×10^{18}, and 5.5×10^{17} atoms/cm^3, respectively, and all decay to background levels within 50 nm of the epitaxial layers. The lower oxygen concentration peak of density ~5×10^{17} cm^{-3} at the AlN buffer/substrate interface is attributed to the *in situ* Al-polishing, which reduces the oxygen level at the AlN homoepitaxy growth interface. This effect was confirmed by SIMS analysis in our previous study.[29,30]

For comparison, SIMS analysis was also conducted on an undoped AlN/GaN/AlN sample, as shown in Fig. S2 in the supplementary material, revealing the presence of unintentionally incorporated impurities. In the shallow SIMS profile [see Fig. S2(b)], a spike in oxygen concentration is observed at the bottom GaN/AlN interface, likely caused by the growth interruption after the AlN

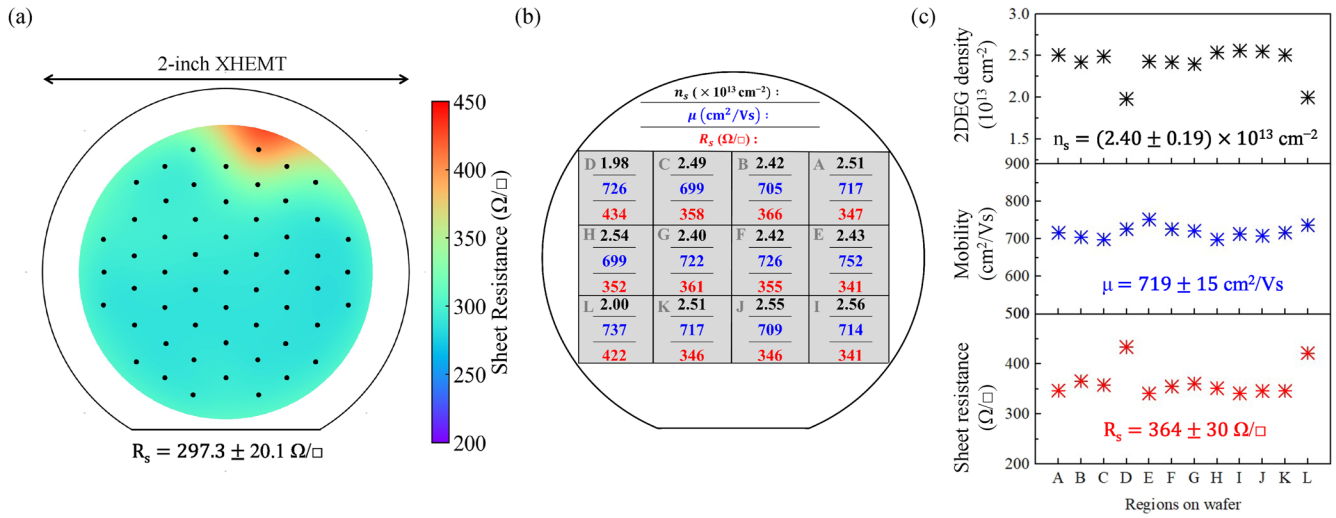

FIG. 6. Transport properties of the δ-doped AlN/GaN/AlN on a 2-in. single crystal AlN substrate. (a) Contactless sheet resistance mapping reveals a uniform sheet resistance of 297.3 ± 20.1 Ω/□ across the 2-in. wafer. Measurements were taken at 55 points (block dots) across the wafer, up to a radius of 0.69 in. (b) 12 1 × 1 cm^2 samples were diced for Hall-effect measurements, performed using a Nanometrics HL5500 system in a standard Van der Pauw geometry. (c) A statistical summary of the Hall-effect measurements on 12 1 × 1 cm^2 samples reveals a 2DEG density of $n_s = (2.40 \pm 0.19) \times 10^{13}$ cm^{-2}, a mobility of $\mu = 719 \pm 15$ cm^2/Vs, and a sheet resistance of 364 ± 30 Ω/□.

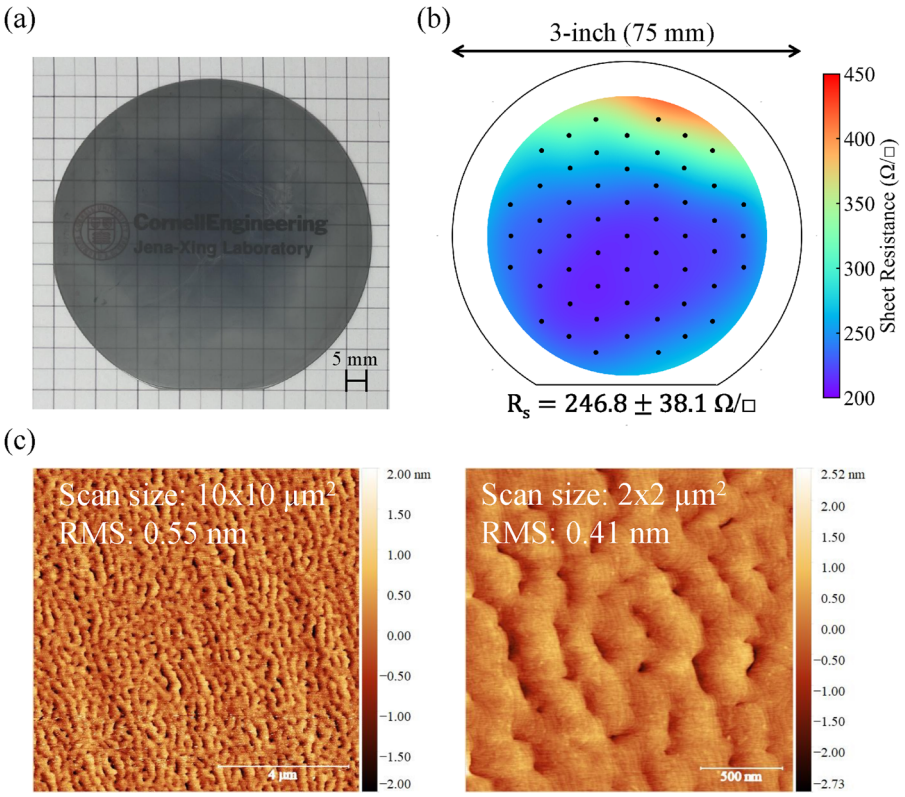

FIG. 7. (a) Optical image of the δ-doped AlN/GaN/AlN heterostructure grown on a 3-in. (75 mm) single-crystal AlN substrate. (b) Contactless sheet resistance mapping shows a uniform sheet resistance of 246.8 ± 38.1 Ω/□ across the 3-in. wafer. Measurements were taken at 55 points (block dots) across the wafer, up to a radius of 1.04 in. (c) AFM scans over 10 × 10 and 2 × 2 μm^2 areas reveal smooth surface morphologies with atomic step features.

buffer. A peak in silicon concentration is also detected at this interface, which is expected from a thermodynamic perspective: under Al-rich conditions, silicon accumulates at the AlN buffer's growth front and subsequently incorporates into the crystal by substituting on Ga sites as GaN begins to grow. In the undoped structure, SIMS analysis reveals an unintentionally incorporated silicon concentration of $\sigma_\delta = 8.7 \times 10^{12}$ cm^{-2} at the bottom GaN/AlN interface.

Figures 6(a)–6(c) show the transport properties of the 2-in. XHEMT wafer. Figure 6(a) shows a contactless sheet resistance map obtained using a Lehighton Electronics' LEI-1320 instrument. Measurements were taken at 55 points across the wafer, up to a radius of 0.69 in., with each point representing the average over a ~10 mm diameter circular region. The sheet resistance across these points is 297.3 ± 20.1 Ω/□, corresponding to a 6.7% variation. Figure 6(b) shows 12 1 × 1 cm^2 pieces diced from the 2-in. XHEMT wafer, with Hall-effect measurements performed using a Nanometrics HL5500 system in a standard Van der Pauw geometry. Figure 6(c) presents the statistical summary of these measurements. The 2DEG density across these samples is $n_s = (2.40 \pm 0.19) \times 10^{13}$ cm^{-2}, with mobility $\mu = 719 \pm 15$ cm^2/Vs and sheet resistance of 364 ± 30 Ω/□.

Figure 7(a) shows an optical image of the 3-in. (75 mm) XHEMT, grown using MBE under optimized growth conditions. Because of the larger area and transparency of 3-in. AlN substrates, we observed less uniform heat dissipation and more rapid metal droplet desorption compared to growth on 2-in. wafers. This issue could be mitigated by coating the backside with a thermally conductive metal or by increasing the flux during growth. Figure 7(c) presents the surface morphology of the wafer center with a rms roughness of ~0.5 nm. The slightly higher roughness compared to the 2-in. XHEMT may result from reduced metal coverage over the larger wafer area. The contactless sheet resistance mapping of the 3-in. XHEMT, shown in Fig. 7(b), was measured at 55 points across the wafer up to a radius of 1.04 in. The sheet resistance is 246.8 ± 38.1 Ω/□, corresponding to a 15.4% variation. Both 2-in. and 3-in. XHEMT exhibit reasonably uniform sheet resistance across the wafer. The cause of the high sheet resistance region on the opposite side of the primary flat is under investigation. The successful growth of large-area XHEMT heterostructures with high uniformity marks a significant step toward scalable manufacturing of AlN HEMTs for next-generation ultrawide bandgap electronics.

IV. CONCLUSION

In summary, this study presents a comprehensive investigation of the δ-doped AlN/GaN/AlN XHEMT structure on bulk AlN wafers, spanning from atomic-scale insights to the demonstration of scalable, large-area growth. STEM analysis confirmed a coherently strained GaN channel between AlN layers and an atomically sharp interface near the 2DEG. Guided by a self-consistent 1D Schrödinger–Poisson simulation, a series of samples with varying δ-doping densities were grown to study their transport properties. The doping density was systematically varied from $\sigma_\delta = 0$, where a 2DHG is present at the bottom interface, to $\sigma_\delta = 5 \times 10^{13}$ cm^{-2}, where the 2DHG is fully suppressed. Further increase to $\sigma_\delta = 6 \times 10^{13}$ cm^{-2} leads to over-doping, which induces a second parallel 2DEG

channel. XHEMTs achieve a 2DEG density of 2.41×10^{13} cm^{-2}, mobility of 802 cm^2/Vs, and sheet resistance of 323 Ω/□. Finally, we scaled the growth of XHEMTs to 2-in. and 3-in. bulk AlN substrates, achieving smooth surface morphology and uniform sheet resistance of 246.8 ± 38.1 Ω/□ across a 3-in. wafer. These results mark a significant advancement toward the practical implementation of the XHEMT 2DEG platform on bulk AlN wafers for RF and power electronics applications.

DISTRIBUTION STATEMENT

Distribution Statement A: Approved for public release. Distribution is unlimited.

SUPPLEMENTARY MATERIAL

See the supplementary material for the secondary ion mass spectrometry analysis of the undoped AlN/GaN/AlN sample.

ACKNOWLEDGMENTS

This study was primarily supported by NORDTECH NITRIDER, the Microelectronics Commons Program, a DoD initiative, under Award No. N00164-23-9-G061. Partial support was also provided by the Army Research Office under Grant No. W911NF-22-2-0177; ULTRA, an Energy Frontier Research Center funded by the U.S. Department of Energy (DOE), Office of Science, Basic Energy Sciences (BES), under Award No. DE-SC0021230; and the DARPA THREADS program. This study made use of the Cornell Center for Materials Research (CCMR) Shared Facilities, which are supported through the NSF MRSEC program (No. DMR-1719875). The Thermo Fisher Spectra 300 X-CFEG was acquired with support from PARADIM, an NSF MIP (No. DMR-2039380), and Cornell University. N.P. acknowledges support from the National Science Foundation Graduate Research Fellowship under Grant No. DGE2139899.

AUTHOR DECLARATIONS

Conflict of Interest

The authors have no conflicts to disclose.

Author Contributions

Yu-Hsin Chen: Conceptualization (equal); Data curation (lead); Formal analysis (lead); Investigation (lead); Methodology (equal); Validation (lead); Writing – original draft (lead). **Keisuke Shinohara**: Data curation (supporting); Formal analysis (supporting); Methodology (equal); Validation (supporting); Writing – review & editing (supporting). **Jimy Encomendero**: Conceptualization (equal); Data curation (supporting); Formal analysis (supporting); Investigation (supporting); Methodology (equal); Validation (supporting). **Naomi Pieczulewski**: Data curation (supporting); Formal analysis (supporting); Investigation (supporting); Methodology (equal); Validation (supporting); Writing – review & editing (supporting). **Kasey Hogan**: Investigation (supporting); Resources (equal); Writing – review & editing (supporting). **James Grandusky**: Investigation (supporting); Resources (equal). **David A. Muller**: Funding acquisition (lead); Resources (lead); Supervision (lead); Validation (lead). **Huili Grace Xing**: Conceptualization (equal); Funding acquisition (lead); Project administration (lead); Resources (lead); Supervision (lead); Validation (lead); Writing – review & editing (supporting). **Debdeep Jena**: Conceptualization (lead); Funding acquisition (lead); Project administration (lead); Resources (lead); Supervision (lead); Validation (lead); Writing – review & editing (lead).

DATA AVAILABILITY

The data that support the findings of this study are available from the corresponding author upon reasonable request.

REFERENCES

[1] R. Rounds, B. Sarkar, A. Klump, C. Hartmann, T. Nagashima, R. Kirste, A. Franke, M. Bickermann, Y. Kumagai, Z. Sitar, and R. Collazo, "Thermal conductivity of single-crystalline AlN," Appl. Phys. Express **11**, 071001 (2018).
[2] R. T. Bondokov, S. P. Branagan, N. Ishigami, J. Grandusky, T. Nagatomi, K. Tatsuta, T. Miebach, and J. J. Chen, "Two-inch aluminum nitride (AIN) single crystal growth for commercial applications," ECS Trans. **104**, 37 (2021).
[3] R. Dalmau, S. Kirby, J. Britt, and R. Schlesser, "Mapping analysis of crystalline perfection and UV-C transparency of 2-in. aluminum nitride substrates grown by physical vapor transport," Phys. Status Solidi B **261**, 2300482 (2024).
[4] R. T. Bondokov, K. Hogan, G. Q. Norbury, J. Mark, S. P. Branagan, N. Ishigami, J. Grandusky, and J. J. Chen, "(Invited) development of 3-inch AlN single crystal substrates," ECS Trans. **109**, 13 (2022).
[5] R. T. Bondokov, K. Hogan, G. Q. Norbury, S. Matsumoto, and J. Grandusky, "Development of 100 mm AlN single-crystal growth and subsequent substrate preparation," Phys. Status Solidi B **178**, 2500032 (2025).
[6] Z. Zhang, M. Kushimoto, T. Sakai, N. Sugiyama, L. J. Schowalter, C. Sasaoka, and H. Amano, "A 271.8 nm deep-ultraviolet laser diode for room temperature operation," Appl. Phys. Express **12**, 124003 (2019).
[7] X. Hu, J. Deng, N. Pala, R. Gaska, M. S. Shur, C. Q. Chen, J. Yang, G. Simin, M. A. Khan, J. C. Rojo, and L. J. Schowalter, "AlGaN/GaN heterostructure field-effect transistors on single-crystal bulk AlN," Appl. Phys. Lett. **82**, 1299 (2003).
[8] M. Qi, G. Li, S. Ganguly, P. Zhao, X. Yan, J. Verma, B. Song, M. Zhu, K. Nomoto, H. G. Xing, and D. Jena, "Strained GaN quantum-well FETs on single crystal bulk AlN substrates," Appl. Phys. Lett. **110**, 063501 (2017).
[9] S. Ozaki, J. Yaita, A. Yamada, Y. Kumazaki, Y. Minoura, T. Ohki, N. Okamoto, N. Nakamura, and J. Kotani, "First demonstration of X-band AlGaN/GaN high electron mobility transistors using free-standing AlN substrate over 15 W mm^{-1} output power density," Appl. Phys. Express **14**, 041004 (2021).
[10] J. Kotani, J. Yaita, K. Homma, S. Ozaki, A. Yamada, M. Sato, T. Ohki, and N. Nakamura, "24.4 W/mm X-band GaN HEMTs on AlN substrates with the LPCVD-grown high-breakdown-field SiN_x layer," IEEE J. Electron Dev. Soc. **11**, 101–106 (2023).
[11] M. Wolf, F. Brunner, C. Last, H. Halhoul, D. Rentner, E. B. Treidel, J. Würfl, and O. Hilt, "1.17 GW/cm^2 AlN-based GaN-channel HEMTs on mono-crystalline AlN substrate," IEEE Electron Device Lett. **45**, 1048–1051 (2024).
[12] E. Kim, Y.-H. Chen, J. Encomendero, D. Jena, and H. G. Xing, "AlN/GaN/AlN HEMTs on bulk AlN substrates with high drain current density >2.8 A/mm and average breakdown field >2 MV/cm," in *2024 Device Research Conference (DRC)* (IEEE, 2024), pp. 1–2.
[13] A. Yoshikawa, T. Kumabe, S. Sugiyama, M. Arai, J. Suda, and H. Amano, "Characteristics of 2DEG generated at the heterointerface of an AlN/GaN structure grown on an AlN substrate using metal organic vapor phase epitaxy," J. Appl. Phys. **137**, 195303 (2025).
[14] G. Alvarez-Escalante, R. Page, R. Hu, H. G. Xing, D. Jena, and Z. Tian, "High thermal conductivity and ultrahigh thermal boundary conductance of homoepitaxial AlN thin films," APL Mater. **10**, 011115 (2022).
[15] R. Chaudhuri, K. Bothe, A. Lucero, A. Hickman, S. Miller-Murthy, D. Jena, H. G. Xing, and K.-T. Lee, "MOCVD-grown, ultra-thin barrier AlN/GaN/AlN HEMTs fabricated using commercial GaN foundry process for Ka-band operation," Appl. Phys. Express **18**, 076501 (2025).

[16]H. Sena, M. Lawton Siukola Thurston, C. Meng, and S. Chowdhury, "Systematic investigation of AlGaN channels on AlN/sapphire substrates using metal–organic chemical vapor deposition (MOCVD): Toward higher crystallinity and lower surface roughness," APL Mater. **13**, 051111 (2025).
[17]S. Chen, Q. Chen, F. Ye, G. Gao, L. Chen, J. Lin, M. Cao, J. Ye, and W. Guo, "Epitaxial growth of a high-quality GaN/AlN heterostructure for the development of an AlN-back barrier high-electron-mobility-transistor," CrystEngComm **27**, 4011–4018 (2025).
[18]Z. Zhang, J. Encomendero, R. Chaudhuri, Y. Cho, V. Protasenko, K. Nomoto, K. Lee, M. Toita, H. G. Xing, and D. Jena, "Polarization-induced 2D hole gases in pseudomorphic undoped GaN/AlN heterostructures on single-crystal AlN substrates," Appl. Phys. Lett. **119**, 162104 (2021).
[19]J. Yaita, K. Fukuda, A. Yamada, T. Iwasaki, S. Nakaharai, and J. Kotani, "Improved channel electron mobility through electric field reduction in GaN quantum-well double-heterostructures," IEEE Electron Device Lett. **42**, 1592–1595 (2021).
[20]Y.-H. Chen, J. Encomendero, C. Savant, V. Protasenko, H. G. Xing, and D. Jena, "Electron mobility enhancement by electric field engineering of AlN/GaN/AlN quantum-well HEMTs on single-crystal AlN substrates," Appl. Phys. Lett. **124**, 152111 (2024).
[21]S. Rajan, A. Chini, M. H. Wong, J. S. Speck, and U. K. Mishra, "N-polar GaN/AlGaN/GaN high electron mobility transistors," J. Appl. Phys. **102**, 044501 (2007).
[22]M. H. Wong, U. Singisetti, J. Lu, J. S. Speck, and U. K. Mishra, "Anomalous output conductance in N-polar GaN high electron mobility transistors," IEEE Trans. Electron Devices **59**, 2988–2995 (2012).
[23]S. C. Binari, K. Ikossi, J. A. Roussos, W. Kruppa, D. Park, H. B. Dietrich, D. D. Koleske, A. E. Wickenden, and R. L. Henry, "Trapping effects and microwave power performance in AlGaN/GaN HEMTs," IEEE Trans. Electron Devices **48**, 465–471 (2001).
[24]R. Vetury, N. Q. Zhang, S. Keller, and U. K. Mishra, "The impact of surface states on the DC and RF characteristics of AlGaN/GaN HFETs," IEEE Trans. Electron Devices **48**, 560–566 (2001).
[25]E. Kim, Y.-H. Chen, N. Pieczulewski, J. Encomendero, D. A. Muller, D. Jena, and H. G. Xing, "XHEMTs on ultrawide bandgap single-crystal AlN substrates," arXiv:2506.16670 (2025).
[26]Y.-H. Chen, J. Encomendero, C. Savant, V. Protasenko, H. G. Xing, and D. Jena, "High conductivity coherently strained quantum well XHEMT heterostructures on AlN substrates with delta doping," Appl. Phys. Lett. **125**, 142110 (2024).
[27]Y.-H. Chen, J. Encomendero, C. F. C. Chang, H. G. Xing, and D. Jena, "Shubnikov–de Haas oscillations of 2DEGs in coherently strained AlN/GaN/AlN heterostructures on bulk AlN substrates," Appl. Phys. Lett. **126**, 202101 (2025).
[28]E. Kim, Y.-H. Chen, K. Shinohara, T.-s. Nguyen, J. Encomendero, D. Jena, and H. G. Xing, "4.2 W/mm at 10 GHz in silicon delta-doped AlN/GaN/AlN pseudomorphic HEMTs with PECVD SiN passivation," IEEE Electron Device Lett. **46**, 1729–1732 (2025).
[29]K. Lee, Y. Cho, L. J. Schowalter, M. Toita, H. G. Xing, and D. Jena, "Surface control and MBE growth diagram for homoepitaxy on single-crystal AlN substrates," Appl. Phys. Lett. **116**, 262102 (2020).
[30]Y. Cho, C. S. Chang, K. Lee, M. Gong, K. Nomoto, M. Toita, L. J. Schowalter, D. A. Muller, D. Jena, and H. G. Xing, "Molecular beam homoepitaxy on bulk AlN enabled by aluminum-assisted surface cleaning," Appl. Phys. Lett. **116**, 172106 (2020).
[31]A. Yoshikawa, T. Nagatomi, K. Nagase, S. Sugiyama, and L. J. Schowalter, "Pseudomorphic growth of a thin-GaN layer on the AlN single-crystal substrate using metal organic vapor phase epitaxy," Jpn. J. Appl. Phys. **63**, 060903 (2024).
[32]J. H. Davies, *The Physics of Low-Dimensional Semiconductors: An Introduction* (Cambridge University Press, 1998).
[33]B. L. Gelmont, M. Shur, and M. Stroscio, "Polar optical-phonon scattering in three- and two-dimensional electron gases," J. Appl. Phys. **77**, 657–660 (1995).
[34]U. Singisetti, M. Hoi Wong, and U. K. Mishra, "Interface roughness scattering in ultra-thin N-polar GaN quantum well channels," Appl. Phys. Lett. **101**, 012101 (2012).
[35]R. K. Jana and D. Jena, "Stark-effect scattering in rough quantum wells," Appl. Phys. Lett. **99**, 012104 (2011).
[36]D. Jena, *Polarization Induced Electron Populations in III-V Nitride Semiconductors: Transport, Growth, and Device Applications* (University of California, Santa Barbara, CA, 2003).
[37]Y. Zhang, I. P. Smorchkova, C. R. Elsass, S. Keller, J. P. Ibbetson, S. Denbaars, U. K. Mishra, and J. Singh, "Charge control and mobility in AlGaN/GaN transistors: Experimental and theoretical studies," J. Appl. Phys. **87**, 7981–7987 (2000).
[38]M. J. Kane, N. Apsley, D. A. Anderson, L. L. Taylor, and T. Kerr, "Parallel conduction in GaAs/$Al_xGa_{1-x}As$ modulation doped heterojunctions," J. Phys. C: Solid State Phys. **18**, 5629 (1985).

From atomic-scale understanding to wafer-scale growth: delta-doped AlN/GaN/AlN XHEMTs on single-crystal AlN by molecular beam epitaxy

Yu-Hsin Chen,[1] Keisuke Shinohara,[2] Jimy Encomendero,[3] Naomi Pieczulewski,[1] Kasey Hogan,[4] James Grandusky,[4] David A. Muller,[5,6] Huili Grace Xing,[1,3,6] and Debdeep Jena[1,3,6]

[1)] *Department of Materials Science and Engineering, Cornell University, Ithaca, NY, 14853, USA*

[2)] *Teledyne Scientific Company, LLC, Thousand Oaks, CA, 91360, USA*

[3)] *School of Electrical and Computer Engineering, Cornell University, Ithaca, NY, 14853, USA*

[4)] *Crystal IS, Inc., Green Island, NY, 12183, USA*

[5)] *School of Applied and Engineering Physics, Cornell University, Ithaca, New York, 14853, USA*

[6)] *Kavli Institute at Cornell for Nanoscale Science, Cornell University, Ithaca, NY, 14853, USA*

(*Electronic mail: djena@cornell.edu)

(*Electronic mail: yc794@cornell.edu)

SUPPLEMENTARY MATERIAL

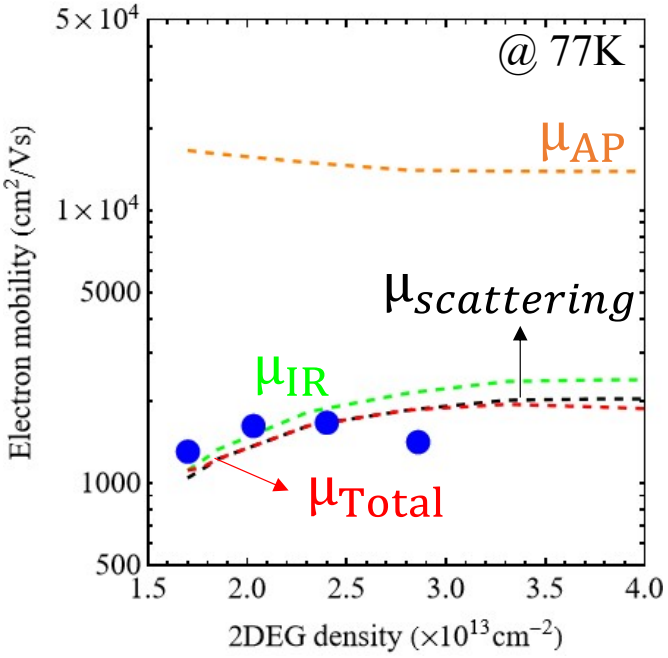

Fig. S1: Theoretical modeling of mobility vs 2DEG density at 77 K for δ-doped AlN/GaN/AlN. At 77K, mobility is primarily limited by IR (μ_{IR}, green lines) and AP (μ_{AP}, orange lines) scattering. The initial increase in mobility as 2DEG density (or δ-doping density) increases is due to the decrease in IR scattering. The decrease in mobility at high 2DEG density is possibly due to parallel conduction from the second electron channel. The discrepancy is due to parallel conduction modeling, where the mobility of the second electron channel is treated as a fitting parameter.

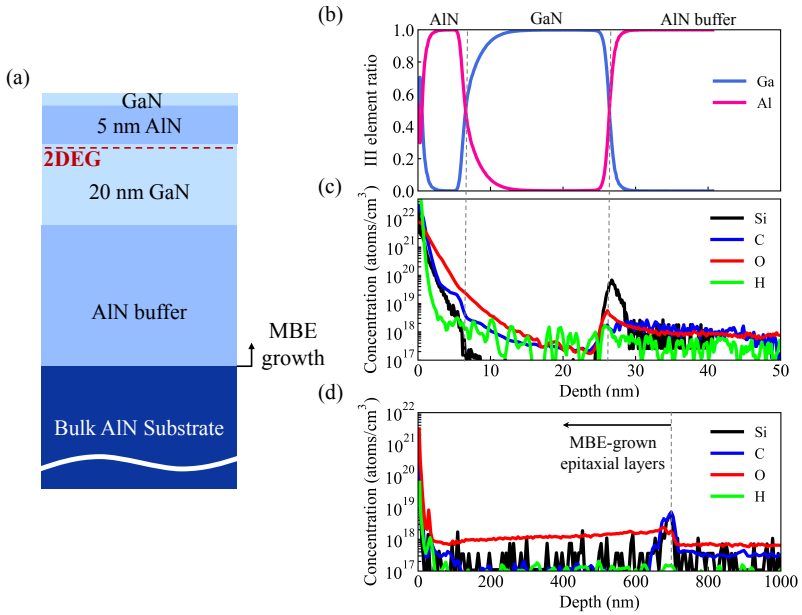

Fig. S2: (a) Schematic of the undoped AlN/GaN/AlN heterostructure on a bulk AlN substrate. Secondary ion mass spectrometry (SIMS) analysis of the undoped sample shows: (b) the group III element ratio, (c) impurity concentrations in the channel region (shallow profile down to 50 nm), and (d) impurity concentrations in the deep profile extending into bulk AlN substrate. SIMS analysis reveals an unintentionally incorporated silicon concentration of $\sigma_\delta = 8.7 \times 10^{12}$ cm^{-2} at the bottom GaN/AlN interface.